Check for updates

ADVANCED MATERIALS
www.advmat.de

Long-Cycling Sulfide-Based All-Solid-State Batteries Enabled by Electrochemo-Mechanically Stable Electrodes

*Daxian Cao, Xiao Sun, Yejing Li, Alexander Anderson, Wenquan Lu, and Hongli Zhu**

The anode plays a critical role relating to the energy density in all-solid-state lithium batteries (ASLBs). Silicon (Si) and lithium (Li) metal are two of the most attractive anodes because of their ultrahigh theoretical capacities. However, most investigations focus on Li metal, leaving the great potential of Si underrated. This work investigates the stability, processability, and cost of Si anodes in ASLBs and compares them with Li metal. Moreover, single-crystal $LiNi_{0.8}Mn_{0.1}Co_{0.1}O_2$ is stabilized with lithium silicate (Li_2SiO_x) through a scalable sol–gel method. ASLBs with a cell-level energy density of 285 Wh kg^{-1} are obtained by sandwiching the Si anode, the thin sulfide solid-state electrolyte membrane, and the interface stabilized $LiNi_{0.8}Mn_{0.1}Co_{0.1}O_2$. The full cell delivers a high capacity of 145 mAh g^{-1} at C/3 and maintains stability for 1000 cycles. This work inspires commercialization of ASLBs on a large scale with exciting manufacturing lines for large-scale, safe, and economical energy storage.

1. Introduction

Great efforts have been made to develop all-solid-state lithium batteries (ASLBs) because of their attractive nonflammability and potentially high energy densities.[1] Among various superionic conductors, sulfide solid-state electrolytes (SEs) exhibit exceedingly high room-temperature ionic conductivities (>1 mS cm^{-1}), enabling ASLBs to work without extra heating.[2] However, sulfide SEs suffer from a narrow electrochemical stability window (1.7–2.3 V, vs Li$^+$/Li) and high reactivity toward many conventional electrodes, such as transition metal oxide cathodes and a Li-metal anode.[3] To achieve energy densities comparable to or even higher than commercial lithium-ion batteries, it is important to select electrodes that exhibit both high energy density and compatibility with sulfide SEs.[4]

The anode material determines the energy density of an ASLB. Indium (In) and an In–Li alloy are the most commonly employed anodes in sulfide SE-based ASLBs due to their excellent stability with sulfide and constant electrochemical potential. However, the high redox potential of ≈0.6 V (vs Li$^+$/Li), high density (7.31 g cm^{-3}), and high cost ($150 000 ton^{-1}) of In make their use challenging in industrial applications.[5] Another anode option, commercial graphite, has the disadvantage of a low specific capacity (372 mAh g^{-1}). As a result, tremendous efforts are being made to seek other promising anode candidates, including conversion, alloy, and intercalation types.[6] Among them, Li metal and Si are two of the most attractive anode materials due to their ultrahigh energy densities.[7]

The Li-metal anode has been investigated since the invention of Li batteries because of its high specific capacity of 3860 mAh g^{-1} and the lowest reduction potential of −3.04 V (vs standard hydrogen electrode). Nevertheless, safety concerns caused by severe dendrite growth have highly restricted its commercialization.[8] For a long time, it was predicted that rigid SEs would revive the use of Li-metal anodes in ASLBs to deliver ultrahigh energy densities. However, studies revealed that using Li metal in ASLBs faces various challenges, such as an unstable interface, low critical current density, and strict operating conditions.[9] When metal sulfides are used as SEs, interface chemical, electrochemical, and mechanical stability between the Li metal and the SE are major concerns. Numerous efforts, like the introduction of an interface protection layer, optimization of SEs to generate a more stable solid electrolyte interphase, and the use of additives in Li metal to adjust the deposition behaviors, have been made to stabilize the interface. However, there is still a long way to commercializing ASLBs coupling a Li-metal anode with sulfide SEs in large-scale manufacturing, as the interface reaction issues and the challenges of integrating Li metal into the existing manufacturing lines still need to be tackled.[10]

As a typical alloy-type anode, Si has an ultrahigh room-temperature theoretical capacity of 3590 mAh g^{-1}, about ten times higher than conventional graphite.[11] The reduction potential is ≈0.4 V (vs Li$^+$/Li) on average, avoiding the risk of Li dendrite formation.[11] Moreover, Si is one of the most abundant elements on Earth and very affordable. The Si anode thus has attracted tremendous interest from industry.[12] However, the commercialization of the Si anode is challenged by its colossal volume change (≈300%) during cycling and low electrical conductivity.[12] The significant volume expansion and contraction

D. Cao, X. Sun, A. Anderson, H. Zhu
Department of Mechanical and Industrial Engineering
Northeastern University
Boston, MA 02115, USA
E-mail: h.zhu@neu.edu
Y. Li, W. Lu
Chemical Science and Engineering Division
Argonne National Laboratory
Lemont, IL 60439, USA
The ORCID identification number(s) for the author(s) of this article can be found under https://doi.org/10.1002/adma.202200401.

DOI: 10.1002/adma.202200401

 © 2022 Wiley-VCH GmbH

create enormous mechanical stresses, causing the electrodes to break and become pulverized. As a result, the battery capacity decays rapidly. Many strategies, such as designing nanostructures, introducing electrolyte additives, optimizing binders, and compositing with other materials, have been proposed to solve the challenges in liquid electrolytes for commercializing the Si anode.[7] However, an investigation of using a Si anode in sulfide SE-based ASLBs has been lacking. Lee et al. studied sulfide SE-based ASLBs using Si composite anodes with Si particle size ranging from nano- to microscales and investigated the effect of carbon additives and external pressure.[13] Takada et al. fabricated thin Si films and applied them in ASLBs.[14] Though excellent rate performance was achieved in these works, the mass loading of active material was low (<0.23 mg cm^{-2}), limiting the energy densities of ASLBs. The ASLBs reported exhibited short cycling life (<100 cycles) and limited cell-level energy density (<225 Wh kg^{-1}, excluding the fraction of current collectors and packages). Meng et al. recently reported a representative work that used pure micro-Si as the anode and the ASLB delivered excellent cycling stability and performance. However, the cell-level energy density is not high due to the employment of a thick SE layer.[15]

In this work, we systematically evaluate the practical application of Si and Li-metal anodes in sulfide SE-based ASLBs. A composite of nano-Si, Li_6PS_5Cl, and carbon conductive was employed as the anode in achieving ASLBs with outstanding cell-level energy densities. The composite anode was prepared through a large-scale ball-milling method and delivered stable cycling performance. We also explore interface coatings on Si, including fabricating ion-conductive and electron-conductive layers. On the cathode side, single-crystal $LiNi_{0.8}Mn_{0.1}Co_{0.1}O_2$ (S-NMC811) was used as the cathode active material. A scalable interface stabilization of S-NMC with a thin layer of lithium silicate (Li_2SiO_x) is adopted to alleviate the side reaction between NMC and sulfide SE. To further increase cell-level energy density and reduce internal resistance, we used a thin—less than 50 µm—SE layer as the ion-conductive membrane. As a result, the ASLBs exhibited remarkable cell-level energy densities of 285 and 177 Wh kg^{-1} at current densities of 0.158 and 3.16 mA cm^{-2}, respectively. When cycled at C/3, the cell delivers a high specific capacity of 145 mAh g^{-1} and maintains stability for 1000 cycles.

2. Results and Discussion

To begin, we designed a high-energy ASLB based on a Si composite anode, a Li_2SiO_x-coated S-NMC (Li_2SiO_x@S-NMC) composite cathode, and a thin sulfide SE membrane, which shows great potential for industrial applications. As illustrated in **Figure 1**A, a sheet-type ASLB was developed. Si nanoparticles were uniformly mixed with carbon black and sulfide SE, creating sufficient electron- and ion-conduction pathways in the anode. In the cathode, a thin layer of Li_2SiO_x coating effectively stabilized the interface between the S-NMC and sulfide SE, contributing to a high capacity. In addition, an ASLB with cell-level high energy density was successfully assembled by utilizing a thin SE membrane. This fabrication could potentially be scaled up to industrial manufacturing, as shown in Figure 1B. Given the excellent air stability of Si, the anode fabrication could be done in a dry room and not limited to a glovebox. In contrast, the Li-metal anode is limited to a glovebox with a high-cost

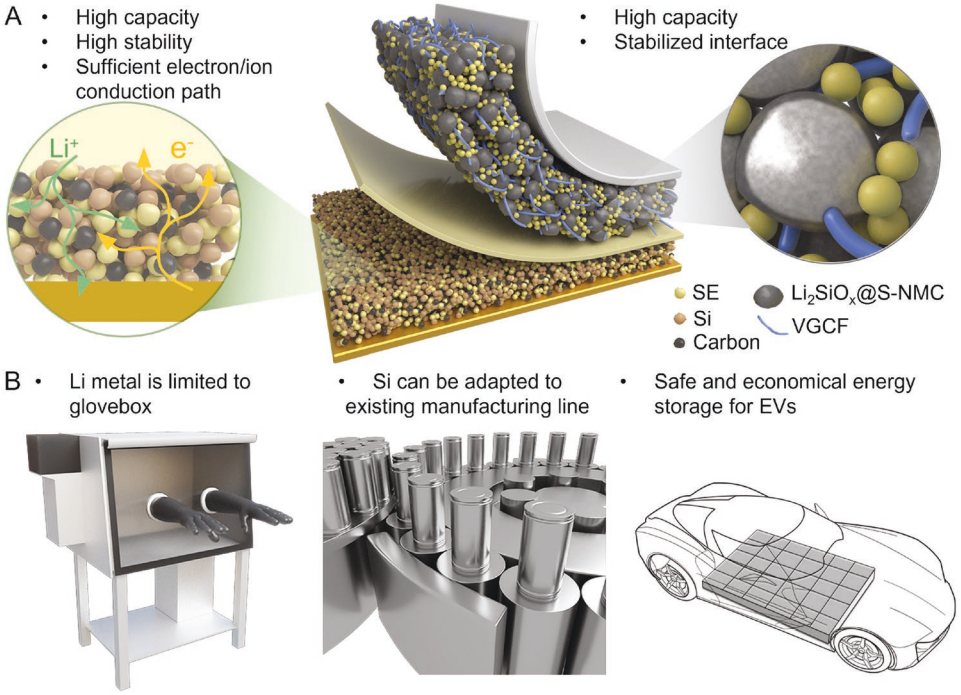

Figure 1. High-energy ASLBs. A) Schematic representations of high-energy ASLBs based on a Si composite anode and Li_2SiO_x@S-NMC composite cathode (A), and the merits of the Si anode and its potential scaling up in industrial manufacturing and applications (B).

© 2022 Wiley-VCH GmbH

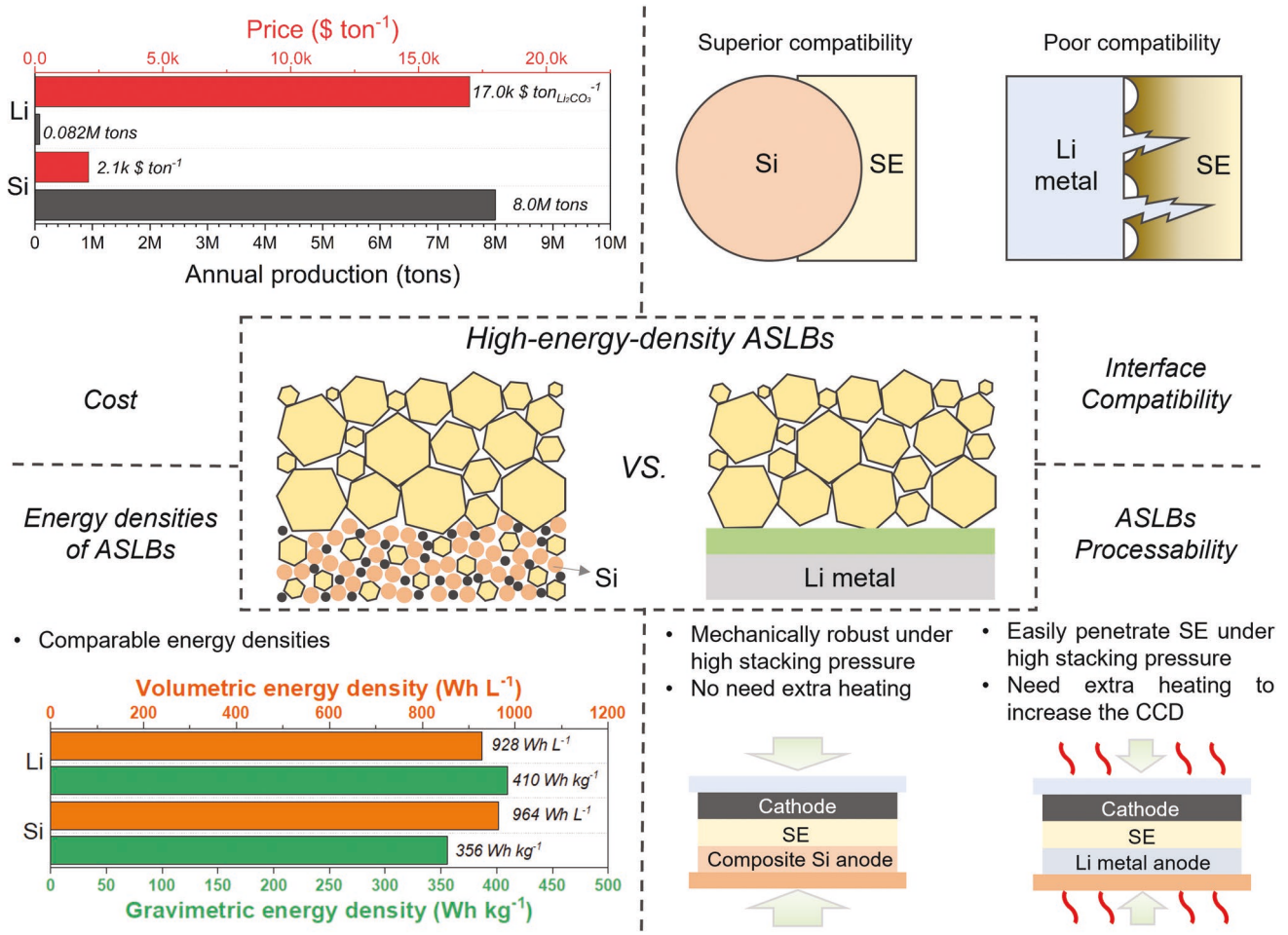

Figure 2. General evaluation of the Si-anode and Li-metal anode. Comparison of the application of sulfide SE-based ASLBs in terms of cost, energy densities of ASLBs, interface compatibility, and ASLBs processability.

Argon atmosphere. With Si as an anode, the fabrication process could easily be carried out in the modified production line for current lithium-ion batteries (LiBs). The Si-anode-based ASLBs have great promise for large-scale energy storage applications, like electric vehicles, as they provide high-energy-density, safe, reliable, long-life, and economically affordable energy storage.

Figure 2 compares the Si anode and Li-metal anode in sulfide SE-based ASLBs from these four perspectives: cost, energy densities, interface compatibility, and processability. First, reducing the cost of batteries is critical for commercialization. Li is not abundant on Earth, with a worldwide annual mine production of only 0.082 million tons in 2020 (excluding US production).[5] As the global demand of batteries significantly rises, the price of battery-grade lithium carbonate has reached as high as \$17 000 ton^{-1} as of 2018.[5] In comparison, Si, on the other hand, is characterized by abundance and low cost. The annual production could reach 8.0 million tons, and the price of Si metal is only \$2100 ton^{-1}.[5] In the long term, the Si anode is considerably cheaper than the Li-metal anode for large-scale, low-cost ASLBs.

Next, we evaluated the energy densities of ASLBs using a Li-metal and Si anode. Excluding the fractions of the current collectors and packing material, the ASLBs using the Si anode exhibited gravimetric and volumetric energy densities of 356 Wh kg^{-1} and 965 Wh L^{-1} respectively, which are comparable to those of the Li-metal anode (410 Wh kg^{-1} and 928 Wh L^{-1}). Note that the calculation is based on experimental results from the literature. Details are shown in Table S1, Supporting Information.

The next step was to compare the compatibility of Si and Li-metal anodes with sulfide SE. Li metal suffers from severe chemical reactions with most sulfide SEs resulting in interphase formation with low ionic conductivities. More seriously, Li metal has intense dendrite growth and very low critical current density (<0.2 mA cm^{-2} for bare Li metal) at room temperature. An interface stabilization is often used between Li metal and sulfide SE, which can be challenging in large-scale manufacturing. In comparison, Si is thermodynamically stable with sulfide SEs, and no passivation coatings are needed to insulate Si from the sulfide SE. The high working potential of Si lowers the dendrite formation risk.

Finally, we evaluated the processibilities of ASLBs using each anode Generally, high stacking pressure is applied in ASLBs fabrication to achieve intimate contact between electrodes and electrolytes.[16] However, under a pressure above 25 MPa, Li metal easily propagates through the SE and causes a short

© 2022 Wiley-VCH GmbH

circuit.[17] In contrast, Si has a high Young's modulus of 130 GPa and is dimensionally stable under high pressure.[18] In addition, Li-metal-based ASLBs usually need extra heating to improve the reaction kinetics and increase the critical current density, but the Si anode exhibits good room-temperature performance even at a high current density. It is also well known that Li is reactive in the ambient environment and must be manufactured inside a glovebox, while Si is stable in the ambient environment for large-scale manufacturing.

What is more important is that the high surface area of Si powder enables mixing the Si with both carbon and SE, which increases the effective electrochemical reaction area, increases the total current density, and reduces local current density. The current density in reported work can reach 10 mA cm^{-2}, demonstrating superior compatibility and potentially higher power.[19] It is challenging to mix Li with SE homogeneously with the Li-metal anode to obtain a similar effect. Even before the challenges in Li metal are addressed, we concluded that the Si anode is highly promising in sulfide SE-based ASLBs for large-scale manufacturing and commercialization.

Si exhibits low electrical conductivity ($<10^{-5}$ S cm^{-1}) and low ion diffusivity.[13] A simple approach to improving the Si anode's performance is to form a composite between it, the SEs, and conductive additives. To demonstrate the processability of the Si anode, we used a simple ball-milling method to synthesize the Si composite anode for ASLBs, as depicted in **Figure 3**A. Si nanoparticles, SE, and carbon black (CB) were mixed in a weight ratio of 6:3:1 through ball milling at 400 rpm for 2 h. Si nanoparticles with a particle size of 50–100 nm were used as the active material, argyrodite-type Li_6PS_5Cl worked as the SE due to its high ionic conductivity of ≈2 mS cm^{-1}, and commercial CB was selected as the conductive additive. Due to the ionically and electronically insulating, a binder is not used in the electrodes. Due to the large contact area between Si with SE and CB, electron- and ion-conduction paths are well established in the whole electrode, which boosts the critical current density of the anode. In contrast, as illustrated in Figure 3B, Li metal experiences a relatively low contact area with SE causing limited critical current density.

Figure 3C shows the scanning electron microscopy (SEM) image of Si nanoparticles with spherical morphology and particle size ranging from 50 to 100 nm. After the ball milling, Si, SE, and CB were uniformly mixed. As depicted in Figure 3D, the Si nanoparticles maintain their spherical morphology and are mixed with a mud-like SE. The homogeneous mixing with SE and CB benefits the ion and electronconduction in the Si anode. Figure 3E reveals the X-ray diffraction patterns of Si, SE, and Si–SE–CB. The nano-Si shows sharp diffraction peaks at 28.4°, 47.3°, 56.1°, 69.1°, and 76.3°, demonstrating a high degree of crystallinity. The Li_6PS_5Cl shows the typical diffraction patterns of argyrodite, and no impurities were found. In Si–SE–CB, all the diffraction peaks are indexed to the crystalline Si and argyrodite Li_6PS_5Cl, demonstrating the chemical stability between Si and SE. Figure S1 in the Supporting Information shows the Raman spectra of Si–SE–CB. No new peaks are found in Si–SE–CB, demonstrating excellent chemical stability among the three components.

The performance of the Si–SE–CB was first investigated in a half cell where In–Li acts as the counter electrode. A current density of 0.1 mA cm^{-2} and voltage range of 0–1.5 V (vs Li^+/Li) were applied. Figure 3F depicts the galvanostatic charge and discharge profiles of the half-cell ASLBs with the Si anode at the first two cycles. High discharge and charge capacities of 2773 and 2373 mAh g^{-1} (corresponding to 2.64 and 2.26 mAh cm^{-2}) were achieved at the first cycle, and the initial coulombic efficiency (ICE) is as high as 85.6%. During the first discharge, one long plateau lower than 0.2 V appears, representing the gradual lithiation process of crystalline Si. In the charging process, there is no apparent plateau, but a slope is found suggesting the complex dealloying of Li ions from different Li–Si alloy (Li_xSi) phases. In the following cycle, the discharge profile is significantly different. The voltage gradually reduces, and a slope with an onset potential higher than 0.25 V is observed, representing the lithiation process of amorphous Si.[11] This demonstrates the amorphization of Si at the first cycle.

The differential capacities with cell potential are plotted to analyze the electrochemical reaction processes further, as shown in Figure 3G. At the first discharge, a prominent peak can be observed at 0.057 V with an onset potential of 0.180 V, corresponding to the plateau in Figure 3F. This process indicates the formation of metastable amorphous Li_xSi by a solid-state amorphization reaction.[20] No pronounced peaks are observed before discharging to 0.2 V, suggesting that the decomposition of SE can be ignored. In the following dealloying process, two broad oxidation peaks at 0.303 and 0.474 V can be observed and are ascribed to the phase transformation from $Li_{3.17}Si$ to Li_7Si_3 and then to LiSi.[21] In contrast, two peaks, at 0.219 and ≈0.01 V at the second discharge process correspond to the converse transformations from LiSi to Li_7Si_3 and then to $Li_{3.17}Si$.[21] The broad peak at 0.219 V signals the alloying process of amorphous Si. The oxidation peak in the following charge process is similar to the first cycle. Figure S2, Supporting Information compares the X-ray diffraction (XRD) of the Si composite anode in pristine, fully discharged, and fully charged states. The dramatically reduced Si peak intensity demonstrates the amorphization process of Si during cycling: The crystalline Si nanoparticles experience an amorphization during the first cycle with the transformation between different Li_xSi phases.

Figure 3H shows the rate performance of the Si composite anode at current densities of 0.1, 0.2, 0.5, 1, and 2 mA cm^{-2}; the corresponding average capacities are 2309, 2122, 1467, 802, and 440 mAh g^{-1}, respectively. Here 2 mA cm^{-2} equals 1.71 C, based on the theoretical room-temperature capacity of 3590 mAh g^{-1}. This current density greatly exceeds most reported critical current density of Li metal toward sulfide SE, demonstrating the superiority of Si to Li metal in the compatibility with sulfide SEs. Figure 3I displays the long-term cycling performance of the Si composite anode at the current density of 0.5 mA cm^{-2}. The ASLB displays remarkable specific discharge and charge capacities of 2067 and 1997 mAh g^{-1} individually. After 200 cycles, there are still ultra-high capacities of 1345 and 1316 mAh g^{-1} remaining. Notably, the counter electrode (In–Li) used here may slightly affect the cycling stability due to the cavities or voids formed at the interface between In–Li and SE at high currents.[22]

The morphology evolution of the composite anode before and after the rate performance was investigated by the SEM

© 2022 Wiley-VCH GmbH

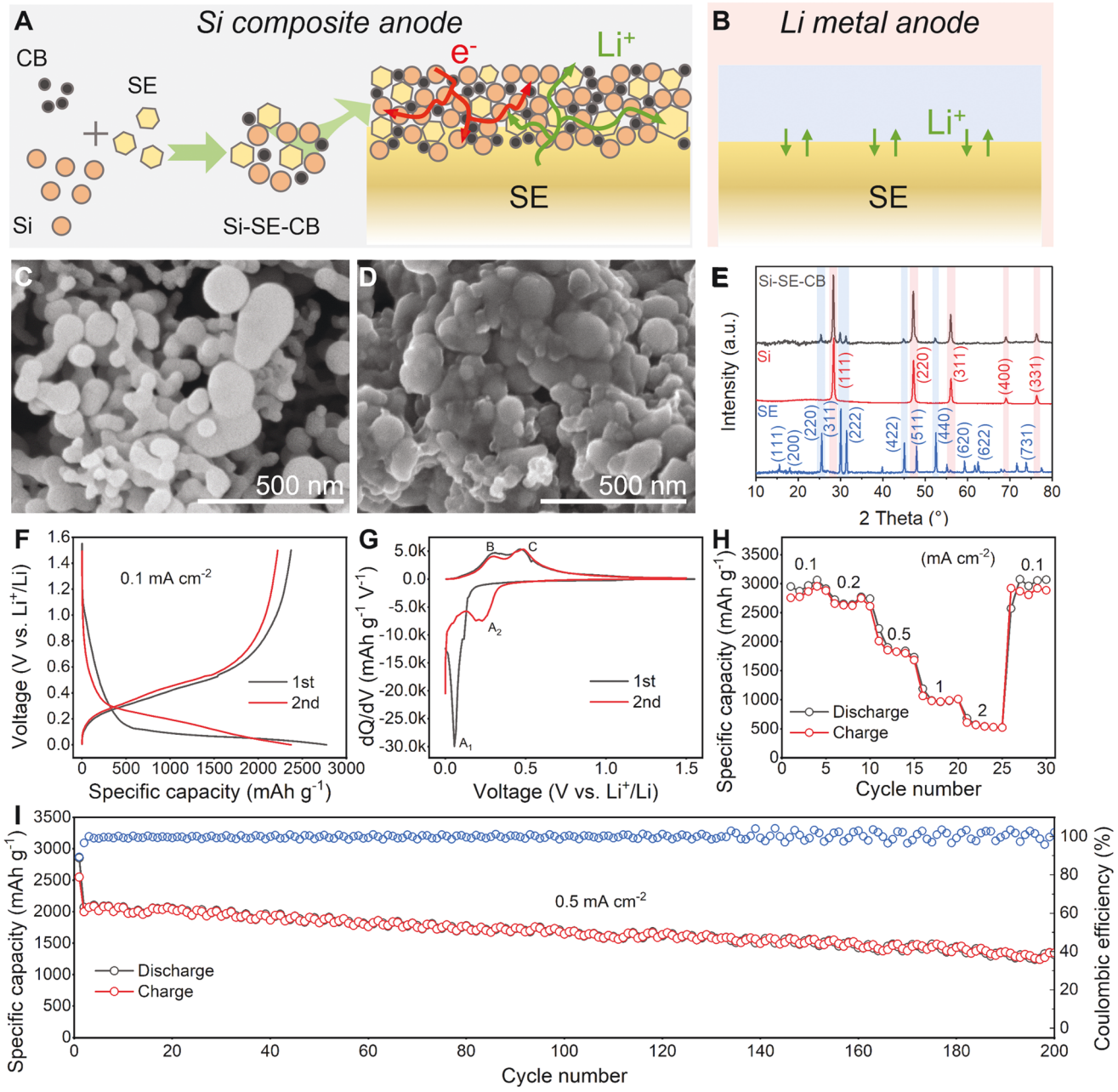

Figure 3. Half-cell performance of the Si anode. A) Schematics of the preparation process of Si–SE–CB and the configuration of Si composite anode in ASLB. The electron- and ion-conduction paths are highlighted. B) Schematic of the Li-metal anode configuration in ASLB and the ion-conduction paths are highlighted. C,D) SEM images of Si nanoparticles (C) and Si–SE–CB (D). E) XRD of Si, SE, CB, and Si–SE–CB. F) Galvanostatic charge and discharge profiles and G) corresponding dQ/dV profiles of ASLB at the first cycle. H) Rate performance of ASLB at current densities of 0.1, 0.2, 0.5, 1, and 2 mA cm^{-2}. I) Long-term cycling performance of ASLB at a current density of 0.5 mA cm^{-2}.

to analyze the electrochemical behavior further. **Figure 4**A shows the top view morphology of the composite anode before cycling. After being stacked on the SE layer at high pressure (300 MPa), the electrode shows a uniformly flat surface without large cracks or voids. When further magnified in Figure 4B, it is clear that the granular Si and the muddy SE–CB matrix are uniformly mixed, and some tiny pores exist in the electrode. The samples were cut with a REXBETI single-edge razor blade to check the cross section morphology. The cross section image in Figure 4C shows that the electrode is well integrated with the SE layer, and no large cracks or voids were observed. After cycling, the morphology varies quite a bit. Figure 4D depicts the top view morphology of the electrode at the same magnification as Figure 4A. The electrode surface is still smooth, but many reticular cracks can be observed. The cracks are longer than 50 µm and less than 1 µm wide (Figure S3, Supporting Information). Though cracks appear, the electrode maintains integrity without breaking. Figure 4E magnifies the surface of

© 2022 Wiley-VCH GmbH

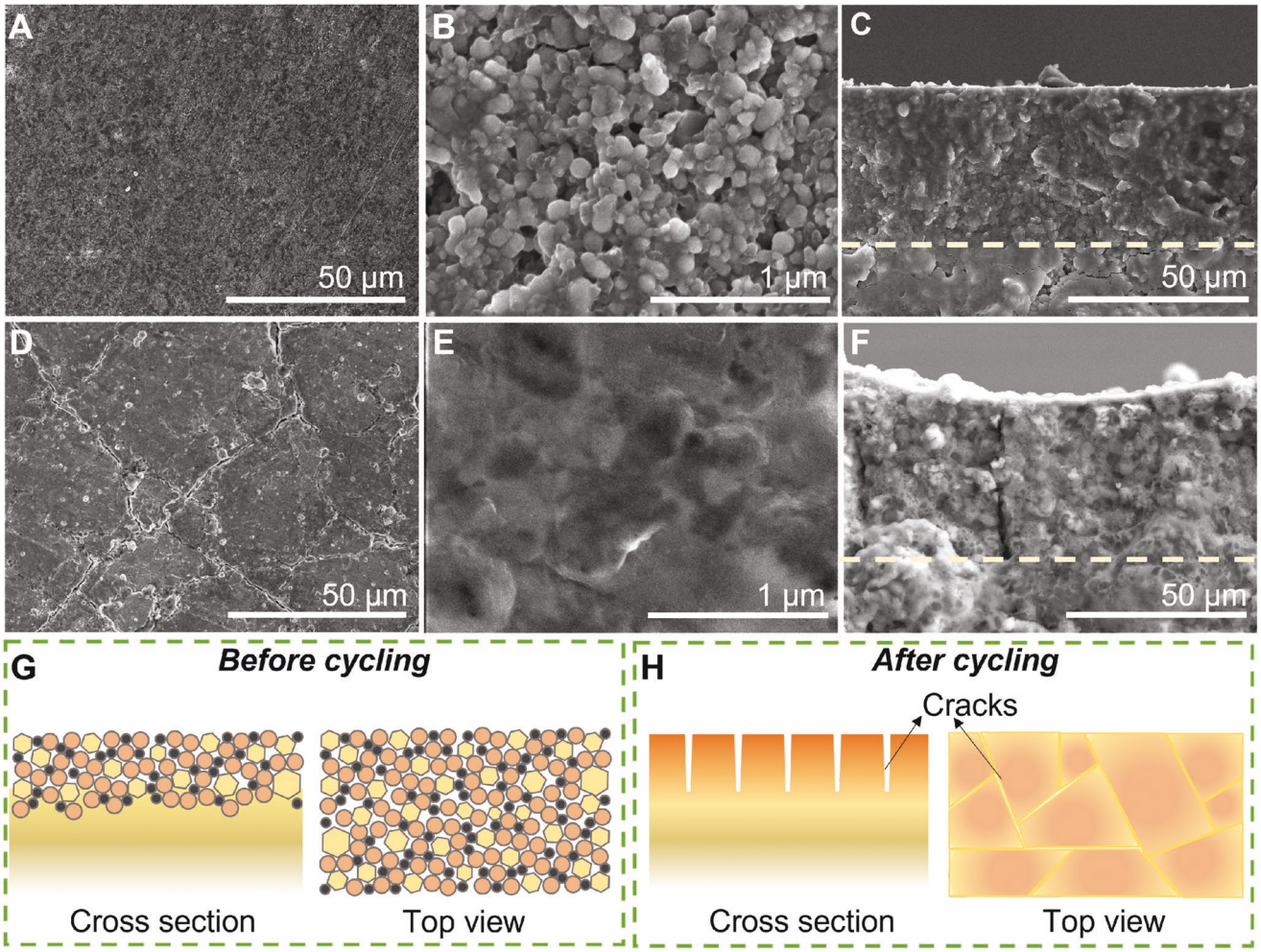

Figure 4. Morphology evolution of the Si anode after cycling. Top-view SEM images of the Si composite anode before cycling in magnification of A) 1000× and B) 10 000×. C) Cross section image of Si composite anode before cycling. Top-view SEM images of the Si composite anode after cycling in magnification of D) 1000× and E) 10000×. F) Cross section image of the Si composite anode after cycling. The vertically generated cracks are highlighted. Schematically illustration of the Si composite anode in cross-section and top view G) before and H) after cycling.

the electrode. Surprisingly, the granules and pores disappear but are replaced with a dense and homogeneous morphology. Figure 4F displays the cross section morphology of the electrode after cycling. There are apparent vertically growing cracks corresponding to the reticular cracks in the top view. However, there is no delamination between the electrode and SE layer, so failure of the ASLB is avoided.

The morphology evolution is schematically illustrated in Figures 4G,H, which show top view and cross-section. After cycling, the granulate morphology of the composite transforms into a dense and homogeneous morphology, while some vertically growing cracks are generated. Based on the electrochemical behaviors, the Si experiences an amorphization during cycling, which explains the transformation in morphology. There are no significant changes in the SEs, indicating that the amorphization of Si likely causes the morphology evolution. This dense and homogeneous electrode gives the Si high electron and ion accessibility and buffers the Si volume expansion, contributing to stable cycling. At the same time, the considerable volume change of Si during alloying and dealloying processes may put great strain on the electrode causing the generation of vertical cracks. These vertical cracks have been reported in ASLBs using micro-Si as the anode, and the gaps are considered to buffer the volume change during the Si lithiation process.[22] The intimate contact between the electrode and SE layer provides sufficient electron and ion conduction, explaining the long-term cycling life of the ASLBs.

External pressure is critical for the Si anode in ASLBs. Two Si-anode half cells were cycled individually under external pressures of 1 and 10 MPa. As shown in Figure S4, Supporting Information, the cell operated under 1 MPa delivered an initial discharge capacity of 1684 mAh g^{-1} with a low ICE of 43.8%, while the cell operated under 10 MPa showed a higher discharge capacity of 2135 mAh g^{-1} and ICE of 56.9%. However, the capacities in both cells decreased quickly. The capacity and cycling stability are lower than those of the cell measured at 50 MPa. Figures S5,S6, Supporting Information show the SEM images of the Si-anode half cells cycled under 1 MPa and 10 MPa, respectively. In the cell measured at 10 MPa, vertical cracks can be observed, and the Si shows an amorphous

© 2022 Wiley-VCH GmbH

morphology at the whole electrode. However, in the cell measured at 1 MPa, the Si anode displays amorphous morphology in the region close to the current collector and nanoparticles in the area close to the SE, demonstrating the nonuniform electrochemical reaction and low utilization of Si during the cycling. This proves that external pressure leads to high Si utilization and cycling stability. However, external pressure settings reduce the cell-level specific energy in practice applications. Therefore, engineering advanced cell designs is needed for sulfide-based ASLBs.

To further investigate the stability of the Si anode and the Li-metal anode during cycling, the evolution of the impedances at different charging states was tracked. Figure S7, Supporting Information displays the discharge profile of the Si anode half cell at 0.25 mA cm^{-2} (the impedance was measured every hour). A 30 min interval was applied before the electrochemical impedance spectroscopy (EIS) test. **Figure 5**A shows the stacked Nyquist plots at various discharge states, and the points at frequencies of 10 and 0.04 Hz are highlighted as dashed lines. EIS spectra maintained a similar shape: a depressed semicircle from 10 to 0.04 Hz and a Warburg tail at low frequencies. Overall, the total resistance first decreases and then increases. The EIS of the In–Li|SE|In–Li and Si–SE–CB|SE|Si–SE–CB symmetric cells are investigated to elucidate the root of the impedances (Figures S8,S9, Supporting Information). In the frequency range from 10 to 0.04 Hz, both In–Li|SE|In–Li and Si–SE–CB|SE|Si–SE–CB show incomplete semicircles corresponding to interface resistances at Si|SE and In–Li|SE. Therefore, the depressed semicircle in the half cell is attributed to the combined interface resistances at the cathode and anode, represented as R_{Int}. Because the grain boundaries exist throughout the cold-pressed sulfide pellet, the depressed semicircles at high frequency are assigned to the grain boundary resistance, $R_{GB.}$ The interception represents the total resistance, $R_{SE,\ bulk}$. Constant phase elements are used to fit the impedance data. The tail at low frequency is attributed to the Warburg region, indicating the ion diffusion in Si.

The EIS spectra are thus fitted with the model of $R(RQ)(RQ)Q$, as shown in the inset of Figure 5B. Significantly, R_{Int} decreases from 101 to 33 Ω in the initial 2 h and gradually increases to 66 Ω after a full lithiation. The enhanced electron conductivity can explain the initial reduction in resistance in Si as partial lithiation. The increased resistance at lower potential has two causes. The first is that the resistance at the In–Li|SE increases when a large portion of Li ions are extracted from the In–Li alloy.[23] The second is the slight decomposition of sulfide SE, which will be further analyzed in the following section. R_{GB} and $R_{SE,bulk}$ show no large difference during cycling.

The cell was then charged, and the EIS was measured at the same conditions (Figure S10, Supporting Information). Figure 5C shows the stacked Nyquist plots during cycling and highlights the points at the 10 and 0.04 Hz frequencies. The Nyquist plots show a shape similar to that of the discharge process. Overall, the total resistance gradually increases as the cell charges. The same equivalent circuit is employed, as shown in Figure 5D. R_{Int} gradually increases from 28 to 42 Ω when the potential is lower than 0.68 V and quickly increases to 148 Ω when the Si is fully delithiated, which can be attributed to the enlarged impedance that occurs when fully extracting Li from Si. Overall, the resistance did not significantly change after one cycle, demonstrating the compatibility between Si and sulfide SE.

The compatibility between Li metal and sulfide SE is investigated in a Li|SE|Li symmetric cell. Figure 5E displays the impedance evolution in the symmetric cell at different rest times before cycling. The resistance gradually increases as the rest time increases, demonstrating the chemical reactions between Li and SE.[24] The cell was then cycled at the same current density as the Si half cell, 0.25 mA cm^{-2}, with a 1 h plating and stripping time for each cycle. As shown in Figure 5F, an overpotential of ≈0.02 V was observed initially; it gradually decreased to 0.006 V after four cycles. Notably, a voltage vibration during cycling demonstrated the unstable interface. The corresponding Nyquist plots after each cycle are compared in Figure 5G. After the first two cycles, there are depressed semicircles observed, indicating the normal working of the symmetric cells. However, the impedance dramatically drops with a negligible capacitive reactance after the third and fourth cycles, highlighted in the inset. This phenomenon indicates a "soft short" in the solid electrolyte, especially in symmetric cells. Figure S11, Supporting Information displays the subsequent cycle performance of the symmetric cell. Though the voltage did not drop to zero, no plate and strip shapes are observed, demonstrating the soft short circuit of the symmetric cell. The critical current density of Li metal against SE was further investigated, as shown in Figure S12, Supporting Information. The value is only 0.5 mA cm^{-2}, which is much lower than that of the Si anode.

X-ray photoelectron spectroscopy (XPS) revealed the stability of the Si composite anode. Figure 5H compares the XPS spectra of the Si 2p region before and after one cycle. In the pristine state, a prominent peak belonging to Si as well as a peak corresponding to Si–O can be observed, suggesting an oxidized layer on the surface of Si nanoparticles. After one cycle, the Si peak decreases significantly, but this is accompanied by a new peak belonging to SiO_2. Since there is no O element source in the electrode, this transformation may be caused by the sample transfer process in XPS measurement. Figure 5I displays the XPS spectrum of S 2p in its pristine state and after one cycle. In the pristine state, the peaks are attributed to the PS_4^{3-} unit of argyrodite-type Li_6PS_5Cl, suggesting good chemical stability between Si and SE. After one cycle, a pair of new peaks belonging to Li_2S appears, demonstrating that the SE experiences a slight decomposition. According to the area ratio of the peaks, only 2.83% of Li_6PS_5Cl degrades after one cycle. The Cl 2p region shows representative peaks of Cl^- ions and no noticeable difference before and after one cycle (Figure 5J). Previous work has proved that Li metal shows poor chemical and electrochemical stabilities with sulfide SE.[2] The Si anode shows much better compatibility with sulfide SE than Li metal, supporting the EIS results and the electrochemical performance.

The cathode plays an equally important role in determining the energy densities of ASLBs. NMC 811 has attracted much attention in industry and academia because of its high discharge capacity of 200 mAh g^{-1}, relatively high average operation voltage of 3.6 V (vs Li^+/Li), and lower cost than the conventional $LiCoO_2$.[25] However, NMC 811 generally exhibits an unsatisfying performance in ASLBs, with low capacity and poor

© 2022 Wiley-VCH GmbH

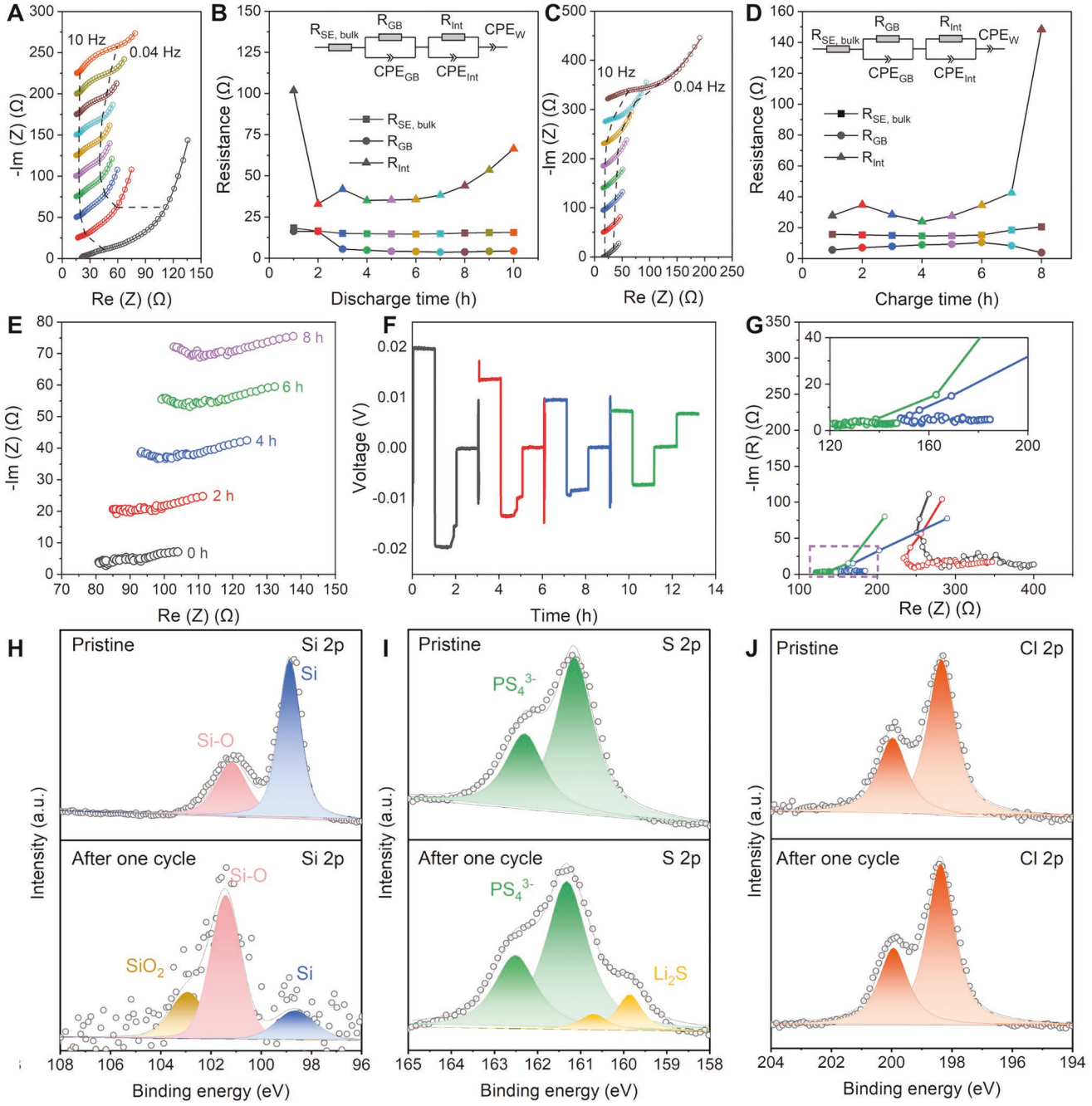

Figure 5. The stability investigation of Si and Li-metal anodes during cycling. A) Stacked Nyquist plots and B) summary of the EIS results of a Si-anode half cell at different discharge states during the first discharge process. C) Stacked Nyquist plots and D) summary of the EIS results for a Si-anode half cell at different charge states during the following charge process. The inset figures in (B) and (D) are the equivalent circuits for EIS fitting. E) Stacked Nyquist plots of the Li|SE|Li symmetric cell at the different resting times before cycling. F) Stripping and plating curves and G) corresponding Nyquist plots after every cycle of the Li|SE|Li symmetric cell at the current density of 0.25 mA cm^{-2}. The inset figure in (G) shows a magnified image of the area highlighted by the dashed rectangle. H–J) XPS spectra of Si 2p (H), S 2p (I), and Cl 2p (J) of a Si composite anode in the pristine state (top) and after one cycle (bottom).

cycling stability. The first cause for this is the unstable interface between sulfide SEs and NMC 811 rooted in chemical and electrochemical reactions.[26] Numerous works have shown that interface engineering that adds an ion-conductive, electron-insulation coating on NMC can effectively address this issue.[27] Another cause is that the nickel-rich NMC used in most ASLBs is polycrystal and suffers from chemomechanical failure during cycling.[28] It has been frequently reported that inner cracks form in the secondary particles of polycrystalline NMC 811.[29] Unlike the flowable liquid electrolyte that can access the inner NMC 811 to maintain a good capacity, SEs can only contact the surface of NMC. As a result, the cracks can dramatically hinder

© 2022 Wiley-VCH GmbH

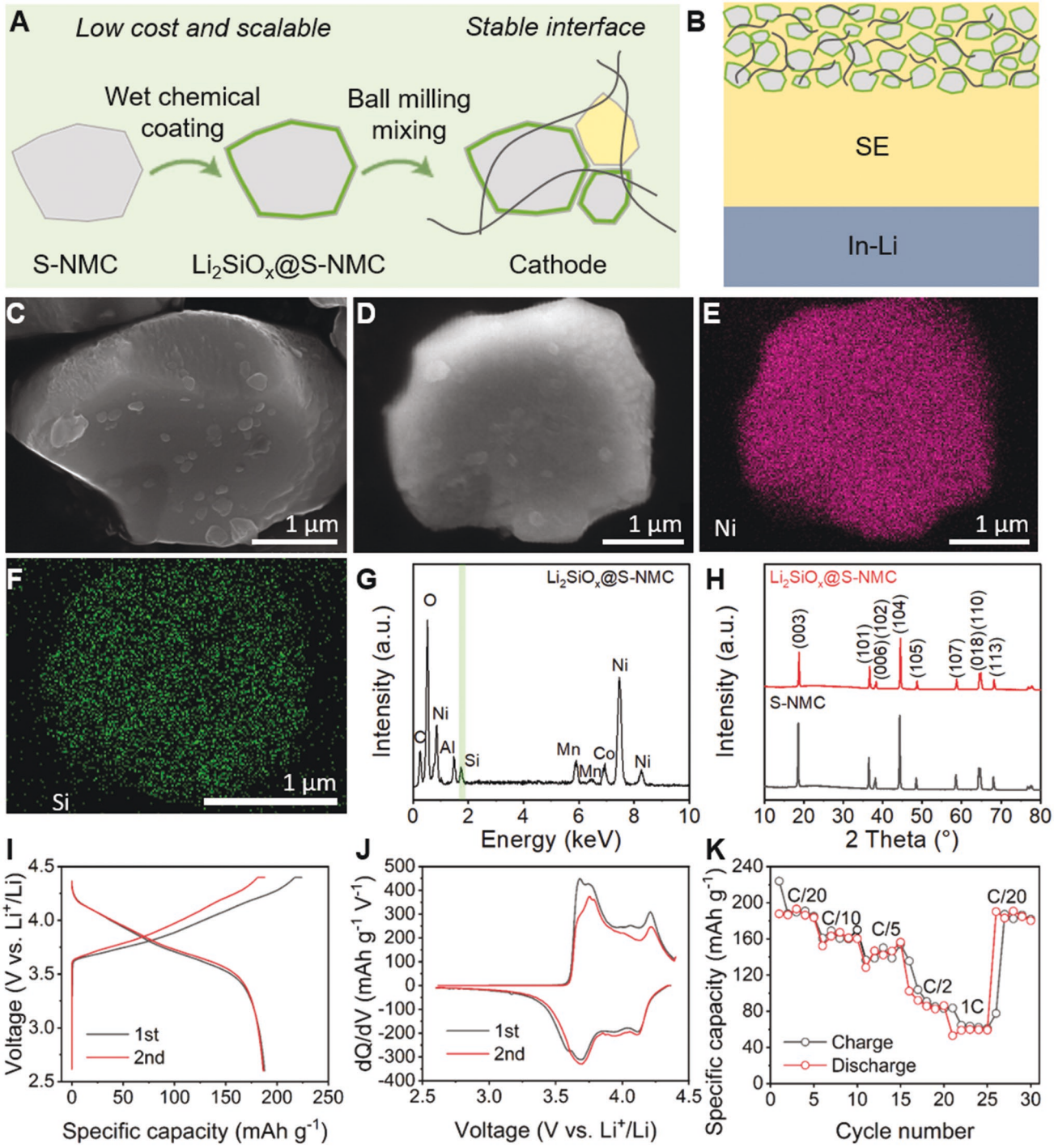

Figure 6. Half-cell performance of Li_2SiO_x@S-NMC cathode. A,B) Schematics of interface engineering on single-crystal NMC 811 to make Li_2SiO_x@S-NMC through the wet chemical coating and the preparation of Li_2SiO_x@S-NMC composite cathode (A), and the configuration of ASLB using a Li_2SiO_x@S-NMC composite cathode and In–Li anode (B). C,D) SEM images of bare S-NMC (C) and Li_2SiO_x@S-NMC (D). E,F) EDX element mappings of Ni (E) and Si (F) in Li_2SiO_x@S-NMC. G) EDX spectrum of Li_2SiO_x@S-NMC to show the presence of Si element. H) XRD of S-NMC and Li_2SiO_x@S-NMC. I) Galvanostatic charge and discharge profiles and J) corresponding dQ/dV profiles of ASLB at the first cycle. K) Rate performances of ASLB at C/20, C/10, C/5, C/2, and 1C. The ASLB was measured at room temperature. Here 1C means 200 mA g^{-1} based on the weight of Li_2SiO_x@S-NMC.

the ion diffusion inside the NMC and result in poor reaction kinetic and, therefore, capacity decay.[30]

To address the above challenges, we developed a Li_2SiO_x-coated single-crystal NMC 811 (abbreviated Li_2SiO_x@S-NMC) using a simple wet chemical coating method, as illustrated in **Figure 6**A. On the one hand, Li_2SiO_x is an promising coating material for industry application. It can effectively alleviate the degradation of SEs and decrease the interfacial resistance,[31]

© 2022 Wiley-VCH GmbH

and it is cheaper than the most popular interface coating material, lithium niobate ($LiNbO_3$). The wet chemical method is scalable and low cost. On the other hand, S-NMC is reported to have fast Li^+ diffusion and eliminated resistance caused by more internal grain boundaries and intergranular fractures than polycrystalline NMC.[32] At the same time, S-NMC is more robust than polycrystalline NMC during mixing and densification, enabling remarkable processibility.[33] Therefore, Li_2SiO_x@S-NMC is a promising high-performance cathode for industry application of sulfide SE-based ASLBs. Mild ball milling was performed to make the composite cathode, a uniform mixture of S-NMC, SE, and conductive additive with a ratio of 80:20:3 in weight. Vapor grown carbon fiber (VGCF) was added to enhance the electron conduction in the composite cathode and maintain the lowest side effect on the degradation of SE. Figure 6B illustrates the architecture of the ASLBs, which use In–Li as a counter electrode to check the electrochemical performance of Li_2SiO_x@S-NMC.

SEM and energy-dispersive X-ray spectroscopy (EDX) mapping were employed to track the Li_2SiO_x coating. Figure 6C shows that the bare S-NMC is a single particle ≈3 µm in diameter, which is a significant contrast to the secondary particles of polycrystalline NMC (Figure S13, Supporting Information). After being coated with 2 wt% of Li_2SiO_x, no noticeable changes were seen in the S-NMC, as shown in Figure 6D. EDX mapping investigation, shown in Figure 6E,F, reveals the uniform distribution of Si and Ni elements, demonstrating that the NMC has been homogeneously coated with Li_2SiO_x. Figure 6G displays the EDX spectrum, where the existence of peak belonging to Si further certifies the coating of Li_2SiO_x. Figure 6H gives the XRD patterns of S-NMC and Li_2SiO_x@S-NMC. All the patterns are attributed to the S-NMC, and no new phases are observed in Li_2SiO_x@S-NMC. This demonstrates that the Li_2SiO_x coating layer is in an amorphous state, and the wet-chemical coating process has no side effects for the S-NMC.

Figure 6I displays the galvanostatic charge and discharge profiles of the half-cell ASLBs using the composite cathode at the first two cycles at the current rate of C/20. Here 1C means 200 mA g^{-1} based on the weight of Li_2SiO_x@S-NMC. The cell was measured between 2.6 and 4.4 V (vs Li^+/Li). High charge and discharge capacities of 224 and 188 mAh g^{-1} were achieved, with a high ICE of 83.9%. After one cycle, no obvious overpotential was observed, and highly reversible charge and discharge capacities of 188 and 186 mAh g^{-1} were obtained at the second cycle. In comparison, the bare S-NMC delivers lower charge and discharge capacities of 212 and 160 mAh g^{-1}, a lower ICE of 75.5%, and increased overpotential (Figure S14, Supporting Information). The outstanding capacity, high ICE, and excellent capacity reversibility are significantly attributed to the interface engineering of Li_2SiO_x on S-NMC and the excellent compatibility between Li_2SiO_x@S-NMC with sulfide SE. Figure 6J depicts the differential capacities with cell potential at the first two cycles. Three pairs of anodic and cathodic peaks are observed at around 3.75 and 3.69 V, 4.05 and 3.94 V, and 4.22 and 4.12 V. The peaks in the low-voltage region are related to the phase transition between monoclinic M and hexagonal H_1 structures. The peaks at the high-voltage region are attributed to the phase transitions among three hexagonal structures, H_1, H_2, and H_3.[34] At the second cycle, no apparent peak shifts can be observed, and the peaks during discharge are almost the same as those of the first cycle, demonstrating stable cycling. In the end, the rate performances of the Li_2SiO_x@S-NMC are evaluated as depicted in Figure 6K. Remarkably, the ASLB delivers average capacities of 187, 160, 144, 90, and 58 mAh g^{-1} at C/20, C/10, C/5, C/2, and 1C, respectively. When recharged at C/20 after 1C, the capacity recovers to 185 mAh g^{-1}, suggesting a highly reversible cycling behavior. Similarly, the counter electrode (In–Li) may affect the performance of ASLB at a high rate.

To demonstrate the promise of the Si anode in ASLBs, we fabricated the full cell using a Li_2SiO_x@S-NMC cathode and Si composite anode. **Figure 7**A illustrates the architecture of the full cell. Here, one piece of 50 µm-thick SE membrane was used as the SE middle layer in the ASLB to achieve a cell-level high energy density. The thin SE membrane has a high ionic conductivity of 1.65 mS cm^{-1} and ultralow areal resistance of 4.32 Ω cm^{-1}, as reported in our previous work.[35] Two kinds of ASLBs were prepared, in which the mass loadings of cathode were 10 and 20 mg cm^{-2}. The n/p ratio was ≈1.35, calculated based on the cathode and anode capacities in half cells. Figures 7B–E present the SEM image and EDX mapping of a cross-section of the full cell with cathode mass loading of 10 mg cm^{-2}. The thickness of the cathode, SE, and anode layer are 62, 50, and 32 µm, respectively. Figure S15, Supporting Information shows the morphology of the composite cathode made of Li_2SiO_x@S-NMC, SE, and VGCF. After uniform mixing, the VGCF builds high electron conduction to the Li_2SiO_x@S-NMC (Figure S15A, Supporting Information). Unlike the relatively loose stack in the cathode, the SE layer is highly dense with no pores, to provide sufficient ion conduction and mechanical strength (Figure S15B, Supporting Information). In the Si composite anode, the Si, SE, and CB are uniformly mixed (Figure S15C, Supporting Information).

Figure 7F presents the galvanostatic charge and discharge profiles of the full cell at the first two cycles at the rate of C/20 (based on the weight of Li_2SiO_x@S-NMC). The mass loading of the cathode is 10 mg cm^{-2}, and the voltage range is between 2.4 and 4.2 V (vs Li^+/Li_xSi). The cell delivers outstanding charge and discharge capacities of 229 and 187 mAh g^{-1} at the first cycle with a high ICE of 81.7%. Unlike the apparent plateau at 3.61 V in the half cell of Li_2SiO_x@S-NMC, the charge profile in the full cell shows a slope with an onset potential of around 2.51 V, which may be attributed to the lithiation of the partially amorphized Si and the slight decomposition of SE. During discharge, the ASLB shows a typical profile for an Si-based full cell with an average potential of 3.39 V. In the following cycle, the charge profile varies a little due to the amorphization of Si during the first cycle, while the discharge profile is almost the same as that in the first cycle demonstrating good stability in the cell. The coulombic efficiency reaches ≈99.9%. Figure 7G shows the differential capacities with cell potentials at the first two cycles. Similarly, there are three pairs of charge and discharge peaks at 3.61 and 3.25 V, 3.93 and 3.63 V, and 4.14 and 3.92 V during the first cycle because of the phase changes of S-NMC. In the second cycle, only the first charge peak shifts to a lower potential of 3.51 V according to the change in charge profiles. Notably, a tiny peak at around 2.57 V is observed in the first cycle but disappears in the second cycle. It suggests that the SE experiences a slight reduction during the first cycle but

© 2022 Wiley-VCH GmbH

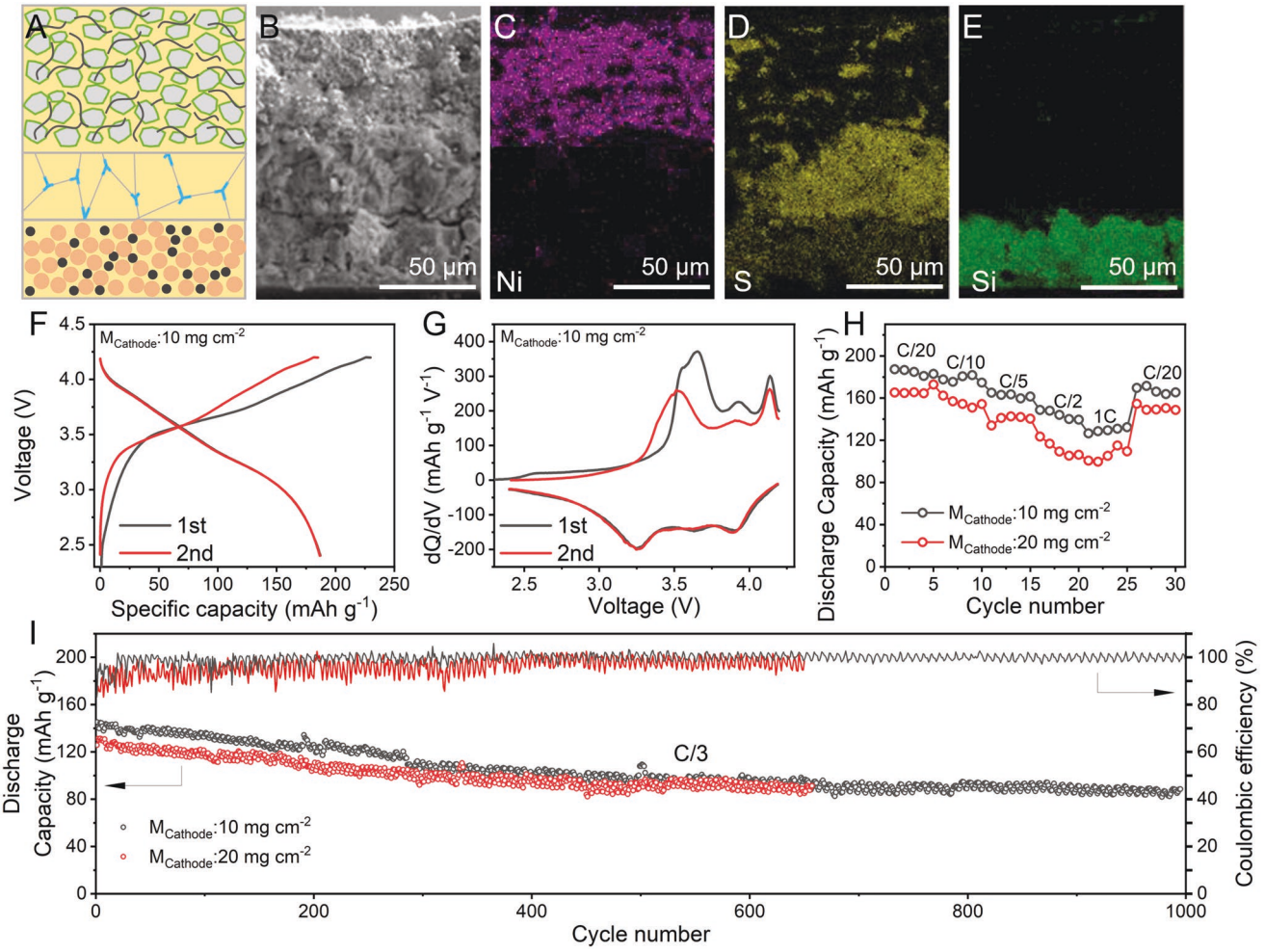

Figure 7. Full-cell performance. A) Schematic of the full cell where a thin SE membrane is utilized. B) SEM image of a cross-section of the full cell. C–E) EDX element mappings of Ni (C), S (D), and Si (E) in the cross section of the full cell. F) The galvanostatic charge and discharge profile of the full cell with cathode mass loading of 10 mg cm^{-2} at first cycle at the rate of C/20, and G) the corresponding dQ/dV profiles. H) Rate performance and I) long-term cycling performance of the full cell with cathode mass loadings of 10 and 20 mg cm^{-2}.

maintains stability in the following cycles. Compared with the half cell of Li_2SiO_x@S-NMC, the ICE decreases from 83.9% to 81.7%, suggesting this side reaction only causes a slight effect.

Figure 7H displays the rate performance of the full cells with cathode mass loading of 10 and 20 mg cm^{-2} labeled as cell I and cell II, respectively. When tested at C/20, C/10, C/5, C/2, and 1C, cell I delivers average capacities of 184, 178, 163, 144, and 130 mAh g^{-1}, respectively. The capacities at high rates are much higher than the half cell of Li_2SiO_x@S-NMC using In–Li as an anode material, demonstrating that the Si anode is better than In–Li at a high current rate. Figure S16, Supporting Information shows the corresponding charge/discharge profiles at different rates, where no huge overpotential was observed, even at 1C. When the mass loading of cathode reaches 20 mg cm^{-2}, cell II maintains high average capacities of 167, 156, 140, 112, and 106 mAh g^{-1} at C/20, C/10 C/5, C/2, and 1C, respectively. Although the mass loading was doubled, the full cell shows negligible overpotential increase at high rates, as shown in Figure S17, Supporting Information. Figure 7I displays the long-term cycling performance of cell I and cell II at the rate of C/3. Impressively, cell I shows a remarkable initial capacity of 145 mAh g^{-1} and maintains stability for 1000 cycles with capacity retention of 62.9%. Cell II shows a lower capacity of 126 mAh g^{-1} in initial and maintains stability for 650 cycles with capacity retention of 71.5%. The regular capacity vibration is caused by the temperature change day and night. Cell I delivered stable coulombic efficiencies of ≈99% over 1000 cycles, and cell II showed lower coulombic efficiencies due to the high mass loading. Figure S18, Supporting Information displays the Raman spectra of the Si anode before and after 1000 cycles. The intensity of Si has significantly decreased, indicating the formation of Li_xSi, which is inactive in Raman.[36] No new peaks can be observed, demonstrating the considerable stability of the sulfide SE in Si composite electrodes in ASLBs.

The cell-level energy densities of the full cells (including only a cathode, SE, and anode) are evaluated to demonstrate the advances of the Si anode. **Figure 8** compares the gravimetric energy densities of the full cells using cathode mass loadings of 10 (star outline) and 20 mg cm^{-2} (solid star) with other reported full cells using Si-related material as an anode at various current

© 2022 Wiley-VCH GmbH

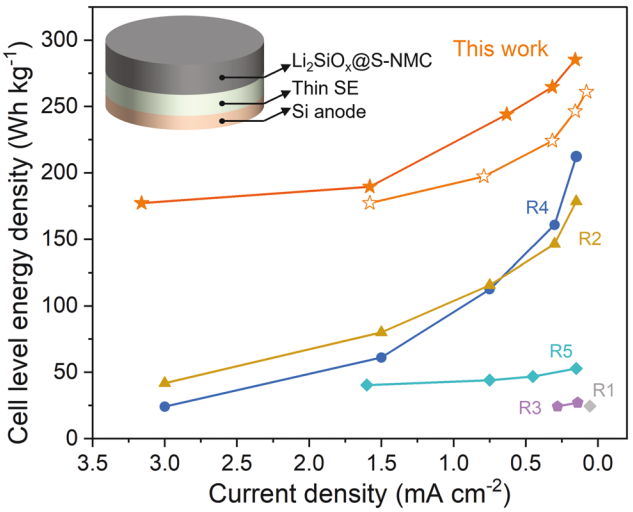

Figure 8. Cell-level energy density evaluation. Cell-level energy density comparison with other reported ASLBs employing a Si anode at various current densities. References S1–S5 are listed in the Supporting Information.

densities. The details of the energy density calculation are listed in Table S2, Supporting Information. Remarkably, the full cell with 20 mg cm^{-2} cathode mass loading delivers the highest energy density, 285 Wh kg^{-1}. Even at the high current density of 3.16 mA cm^{-2}, the energy density is as high as 177 Wh kg^{-1}. Few ASLBs using a Li-metal anode can reach this current density. These outstanding performances show that the Si anode shows greater potential in practical application in ASLBs than Li metal at the current stage.

For the next step—large-scale commercialization—the scaling up of Si-anode-based ASLBs needs further investigation into electrode composition optimization, including adding conductive carbon additive and binder. It has been reported that the carbon additives accelerate the decomposition of SE, and the carbon-free microsilicon (μ-Si) anode enables highly stable ASLBs.[15] Therefore, we evaluated the performance of the pure Si nanoparticles in the full cell. Figure S19, Supporting Information displays the charge and discharge profiles of the ASLBs with pure Si at different rates. The cathode mass loading is 10 mg cm^{-2}, and the n/p ratio is ≈1.3. The cell delivered an initial discharge capacity of 127 mAh g^{-1} with an ICE of 63.2%, much lower than the 184 mAh g^{-1} and 81.7% of the Si composite anode with carbon. Moreover, the full cell with a pure Si anode delivered a low capacity of 81 mAh g^{-1} at 1C, while the full cell with a Si composite anode had a higher value of 130 mAh g^{-1}. This demonstrates that mixing Si with carbon and SE makes for a better utilization of Si, especially at a high rate, which is different from the reported result.[15] One possible reason is that the Si nanoparticles have a larger surface area than the μ-Si, accompanied by more boundaries in pure Si electrodes. There is generally a layer of silicon oxide on the surface of Si nanoparticles which causes a three orders of magnitude reduction in electrical conductivity.[37] As a result, without carbon, the utilization of Si was limited, and the ASLBs delivered poor behavior. This demonstrates that adding carbon in the proper ratio benefits the Si nanoparticle-based ASLBs. In a large-scale application, the addition of binders brings more challenges to the conductivity of the Si anode, so carbon additives are critical in building sufficient electron-conductive pathways, especially in commercialized cells.

Since the intimate physical contact between Si, SE, and CB is challenging in the ASLBs, the effect of interface coating on Si, like the carbon coating (C@Si) and SE coating (SE@C), was also investigated in this work. The carbon coating was conducted through dopamine polymerization and the following carbonization processes. The SE coating was fabricated based on a wet synthesis of $Li_7P_3S_{11}$ (LPS), and the ionic conductivity was around 0.6 mS cm^{-1}. Figure S20, Supporting Information shows the SEM images of C@Si and LPS@Si, which both maintain the morphology of Si nanoparticles. The fraction of the carbon coating is ≈10 wt%, confirmed by thermogravimetry analysis (Figure S21, Supporting Information). The fraction of the LPS is ≈10 wt% controlled by the precursor ratio. C@Si and LPS@Si were mixed with Li_6PS_5Cl and CB in the same formula as Si–SE–CB to prepare C@Si–SE and LPS@Si–SE–CB. Figure S22, Supporting Information shows the half-cell performance of C@Si–SE. An extra electrochemical reaction occurred at 1.091 V, which is attributed to the partial reduction of SE. The enlarged contact between C and SE may accelerate the decomposition of SE.[15] Meanwhile, the carbon coating blocked the ion accessibility to Si. As a result, the cell delivers a low ICE of 57.6%. The LPS@Si–SE–CB shows better performance than C@Si–SE but lower capacity (2689 mAh g^{-1}) and ICE (77.6%) than Si–SE–CB, as shown in Figure S23, Supporting Information. The lower ionic conductivity of LPS than Li_6PS_5Cl can explain this, and the LPS coating may block the electron conduction in the composite anode. The full-cell performances of C@Si–SE and LPS@Si–SE–CB anodes were also investigated. As displayed in Figure S24, Supporting Information, the full cell using the C@Si–SE anode shows deficient capacity (78 mAh g^{-1}), poor ICE (44.8%), and sluggish reaction kinetics. Figure S25, Supporting Information shows the performance of full cells using LPS@Si–SE–CB. A higher capacity of 162 mAh g^{-1} and ICE of 81% is obtained. These results agree with the half-cell performance, demonstrating that a sole carbon or ionic conductor coverage between Si and sulfide electrolyte might block the counterpart charge transfer: pure carbon coating might block ion transfer, and pure ionic conductor coating might block electron transfer.

Another significant issue is the addition of binders. Advanced binders enable electrodes fabrication through film casting, which benefits scaling up and provides better compatibility with the existing manufacturing line of current LiBs.[38] In brief, a binder improves the electrode mechanical stability and benefits ASLBs working at lower external pressure.[39] However, a binder blocks electron and ion transfer and impedes battery performance due to ionic and electronic insulation. In order to minimize these side effects, the binder needs superior binding ability to reduce the amount used. The binder should have excellent electrochemical and chemical stability with both active material and SE. The processing method must also be compatible with sulfide SE which is highly sensitive to moisture and polar solvents.

To demonstrate the scalability of Si anode-based ASLBs, we assembled a 3 × 3 cm^2 pouch cell, as shown in Figure S26,

© 2022 Wiley-VCH GmbH

Supporting Information. The freestanding cathode and SE layer were prepared through dry mixing, using 1 wt% of poly(tetrafluoroethylene) as binder.[39] The anode was prepared using a slurry casting method with 2 wt% of ethyl cellulose used as a binder. The pouch cell was fabricated by stacking Al foil, cathode, SE, and anode/Cu in sequence. The as-prepared pouch cell successfully lit a light bulb. Due to a lack of external pressure, the cell had a large impedance, demonstrating that pressure is critical for Si anode-based ASLBs.

3. Conclusion

In this work, a Si composite anode composed of nano-Si, carbon, and solid electrolyte was successfully prepared using a scalable ball-milling method. The half cell delivers a high capacity of 2773 mAh g^{-1} (corresponding to 2.64 mAh cm^{-2}) with an ICE of 85.6% at 0.1 mA cm^{-2}. The cell also shows a high capacity of 2067 mAh g^{-1} and maintains stability for 200 cycles at 0.5 mA cm^{-2}. Operando EIS measurement reveals that the Si composite anode exhibits better stability during cycling than Li metal. However, the SE has slight decomposition to Li_2S, which possesses descent ionic conductivity for stable cycling. On the other hand, the Li-metal anode suffers severe chemical and electrochemical instabilities with sulfide SE. Furthermore, interface engineering on Si, including carbon coating, ionic conductor coating, and the hybrid coating, were performed. The results revealed that the coating layer impedes the counterpart charge transfer in the Si composite anode and reduces the performance. On the cathode side, a low-cost Li_2SiO_x layer is fabricated on single-crystal NMC 811 to stabilize the interface with sulfide SE. As a result, the full cell employing a nano-Si composite anode, thin SE membrane, and the Li_2SiO_x@S-NMC cathode delivers a remarkable performance: a cell-level energy density of 285 Wh kg^{-1} at a high cathode mass loading of 20 mg cm^{-2}. At a high current density of 3.16 mA cm^{-2}, the energy density at cell level still reaches 177 Wh kg^{-1}. This work sheds light on the commercialization of ASLBs and advances the Si anode in the practical application of ASLBs.

Briefly, the Si anode shows better compatibility with sulfide SE-based ASLBs compared with the Li-metal anode. The Si anode has low cost, remarkable processibility in ASLBs, high critical current density, and promising scale-up. All these merits make the Si anode one of the most promising anodes utilized in ASLBs. Although Li metal has a higher energy density, several challenges, like poor stability, low critical current density, dendrite growth, and strict processing conditions, still limit the commercialization of the Li-metal anode in ASLBs for large-scale industrial manufacturing at the current stage. In the future, the carbon additive, volume expansion, and binder in the Si composite anode are worth more investigations.

4. Experimental Section

Li_6PS_5Cl Preparation: The argyrodite Li_6PS_5Cl was synthesized through a solid-state sintering method. Lithium sulfide (Li_2S, Sigma Aldrich, 99.98%), phosphorus pentasulfide (P_2S_5, Sigma Aldrich, 99%), and lithium chloride (LiCl, Sigma Aldrich, 99%) were mixed in a molar ratio of 2.5:0.5:1 using a 50 mL stainless-steel vacuum for 10 h at 500 rpm in an argon atmosphere. The mixture was sealed in a glass tube and then sintered at 550 °C for 6 h. The obtained sample was then ground in a mortar and stored in a glovebox.

LPS@Si Preparation: The Si powder (Nanostructured and Amorphous Materials, Inc.) was directly used as received without further treatment. The LPS@Si was synthesized through the wet chemical method: 270 mg of Si powders were mixed with 10.7 mg of Li_2S and 19.3 mg of P_2S_5 in 10 mL of acetonitrile with continuous stirring for 24 h at 50 °C. The acetonitrile was then removed in a vacuum. The $L_7P_3S_{11}$@Si was obtained after annealing at 260 °C for 1 h in an Argon-filled glovebox.

C@Si Preparation: The C@Si was synthesized through dopamine polymerization and following carbonization processes: 300 mg of Si powder were mixed with 300 mg of dopamine hydrochloride (Alfa Aesar, >99.0%) in a Tris buffer (300 mL, 10 мм; pH 8.5) and stirred for 12 h. Then polydopamine@Si could be obtained through centrifugation and washing with water three times. The freeze-dried polydopamine@Si was then carbonized in an N_2 filled tube furnace at 400 °C for 2 h with a heating rate of 1 °C min^{-1} and then at 800 °C for 4 h with a heating rate of 5 °C min^{-1}. The C@Si powders were obtained.

Li_2SiO_x Coating on Single-Crystal NMC 811: The coating of Li_2SiO_x on single-crystal NMC 811 was applied using wet-chemical methods. All of the experiments were performed in a glovebox. Tetraethyl orthosilicate (TEOS, Sigma Aldrich, ≥99.0%), lithium (Li, Sigma Aldrich, 99.9%), anhydrous ethanol (Sigma Aldrich), and single-crystal NMC 811 (Nanoramic Inc.) were utilized. Briefly, 3.1 mg of Li was reacted with 1.2 mL of ethanol to form the ethanol solution of lithium ethoxide, and 50 µL of TEOS was then added and stirred for 10 min at 300 rpm. After that, 1 g of NMC powder was mixed into the above solutions and continuously stirred at 300 rpm for 1 h. Then a vacuum was applied to remove the extra ethanol, and bath sonication was maintained to avoid the aggregation of NMC. The dried mixture was heated at 350 °C for 2 h in a muffle furnace with ambient air. The sample obtained was stored in a glovebox for later use.

Materials Characterization: XRD was measured on PANalytical/Philips X'Pert Pro (PANalytical, The Netherlands) with Cu Kα radiation. The samples were sealed with Kapton tape for protection. The Raman spectra were obtained on a Thermo Scientific DXR (Thermo Scientific, USA) with 532 nm laser excitation. The SEM and EDX were conducted on SEM JEOL JSM 7000F (JEOL Ltd., JAPAN). The samples were cut with a REXBETI single-edge razor blade to check the cross section morphology. Thermogravimetric analysis (TGA) was performed on TGA Q50 (TA Instruments Inc., USA) from room temperature to 800 °C at a heating rate of 10 °C min^{-1} in the air. The XPS was conducted on a K-Alpha XPS system (Thermo Scientific, USA).

Si Composite Anode Preparation: All the Si composite anodes were prepared through a simple ball-milling method. For Si–SE–CB, 180 mg of Si powder, 90 mg of Li_6PS_5Cl, and 30 mg of carbon black (acetylene, 99.9+%, Fisher Scientific) were mixed in an argon-filled milling jar (50 mL) at 500 rpm for 5 h. 2 g of ZrO_2 balls (4 mm in diameter) were used. For C@Si–SE, C@Si, and SE were mixed in a ratio of 70:30 by the same method. For LPS@Si–SE–CB, LPS@Si, Li_6PSCl, and CB were mixed in the ratio of 70:20:10 by the same method.

Cathode Preparation: The cathode was prepared through a ball-milling method: 160 mg of Li_2SiO_x@S-NMC powder, 40 mg of Li_6PS_5Cl, and 6 mg of VGCF were mixed in an argon-filled milling jar (50 mL) at 150 rpm for 1 h. 1.2 g of ZrO_2 (4 mm in diameter) was used. The cathode was collected and stored in a glovebox.

Thin SE Layer Fabrication: The fabrication of the thin SE layer was reported in the previous work.[35] In detail, 2 mg of ethyl cellulose was dissolved in 2 mL of toluene at 50 °C. After this was stirred for 2 h, 98 mg of Li_6PS_5Cl powder was dispersed in the solution with continuous stirring at 300 rpm for 2 h. The dispersion was then cast on a vacuum filtration system with a filter diameter of 4.4 cm. A freestanding membrane could be successfully obtained by peeling off the filter paper. The membrane was heated at 150 °C overnight to remove the residual solvent. The thin SE layer was stored in the glovebox for later use.

Half-Cell Fabrication: The half-cell was fabricated in a glovebox (O_2 < 0.1 ppm, H_2O < 0.1 ppm). First, 150 mg of Li_6PS_5Cl powders were

© 2022 Wiley-VCH GmbH

pressed in a polyether ether ketone (PEEK) die (12.7 mm in diameter) under the pressure of 300 MPa. Then 2 mg of composite anodes were cast on one side of the Li_6PS_5Cl pellet, and a piece of In–Li foil (40 mg of In, 1 mg of Li) was stacked on the other side. Copper foil was used as the current collector for both sides. Pressure at 100 MPa was then applied on the die using two stainless steel plugs. Finally, an extra 50 MPa pressure was applied to the cell and maintained by a stainless-steel framework. The Li_2SiO_x@S-NMC half cell was fabricated with a similar method while 10 or 20 mg cm^{-2} of the composite cathode were applied, and In–Li worked as anodes.

Full-Cell Fabrication: The full cell was fabricated based on a thin SE membrane: 10 mg of Si composite anode were first dispersed in 1 mL of toluene, then 200 µL of this dispersion was dropped on the Cu disk (12.7 mm). After being heated at 200 °C for 2 h, the Si composite anode was uniformly cast on the Cu disk. The preparation of the thin SE membrane was reported in the previous work: A piece of thin SE membrane with a diameter of 12.7 mm was placed in the PEEK die (12.7 mm in diameter) and then pressed at 100 MPa. Then the anode disk was stacked on one side, and cathode (10 or 20 mg cm^{-2}) powder was cast on the other side. Al foil was selected as the current collector. The stacked cell was finally pressed at 300 MPa, and an extra pressure of 50 MPa was applied to the cell and maintained by a stainless-steel framework.

Operando EIS Analysis: The operando EIS was conducted on a Biologic SP150 potentiostat (Biologic, France). For the Si anode, the half cell was assembled for measurement. The cell was galvanostatically charged and discharged at the current density of 0.25 mA cm^{-2}. The EIS was measured every hour after 30 min rest. The measurement was carried out at frequencies from 1 MHz to 10 mHz with an AC amplitude of 10 mV. For the Li-metal anode, a symmetric cell was assembled. 150 mg of Li_6PS_5Cl was pressed in the PEEK die at 300 MPa. Then, two pieces of Li-metal foil were stacked on both sides. Cu foil was used as the current collectors. The EIS measurement before cycling was conducted every 2 h. Then the cell was galvanostatically charged and discharged at the current density of 0.25 mA cm^{-2} and limited capacity of 0.25 mAh cm^{-2} for each cycle. The EIS was measured after a rest of 30 min. The setting for EIS was the same as that of the Si anode. ZSimpWin was used for EIS fitting.

Rate and Cycling Performance Measurement: The Si anode half cell was first discharged to –0.6 V and then charged to 0.9 V in constant current density. The specific capacity was calculated based on the weight of Si. The potential of the In–Li foil used here was 0.6 V. The Li_2SiO_x@S-NMC cathode half cell was first charged to 3.8 V at constant current, held at 3.8 V for 1 h, and then discharged to 2.0 V at the same current. The full cell was first charged to 4.2 V at constant current, held at 4.2 V for 1 h, and then discharged to 2.4 V at the same current rate. The specific capacity was calculated based on Li_2SiO_x@S-NMC.

Supporting Information

Supporting Information is available from the Wiley Online Library or from the author.

Acknowledgements

H.Z. acknowledges the financial support from National Science Foundation under Award Number CBET-ES-1924534. The authors acknowledge Dr. Joshua W. Gallaway in the Department of Chemical Engineering to help with the Raman test. The authors would like to acknowledge the Northeastern University Center for Renewable Energy Technology for the use of SEM facilities and providing access to the XRD. The authors also acknowledge the Center for Nanoscale Systems (CNS) Harvard for providing access to the XPS instrument.

Conflict of Interest

The authors declare no conflict of interest.

Author Contributions

H.Z. and D.C. conceived the idea. D.C. and X.S. carried out the main experiments. H.Z. and D.C. collectively wrote the paper. W.L. provided the Si anode. A.A. revised the manuscript. All authors discussed the results. H.Z. supervised the study.

Data Availability Statement

Research data are not shared.

Keywords

all-solid-state batteries, cell-level energy densities, interface engineering, Li-metal anodes, Si anodes

Received: January 13, 2022
Revised: March 21, 2022
Published online: May 10, 2022

[1] X. Yu, A. Manthiram, *Energy Storage Mater.* **2021**, *34*, 282.
[2] a) Q. Zhang, D. Cao, Y. Ma, A. Natan, P. Aurora, H. Zhu, *Adv. Mater.* **2019**, *31*, 1901131; b) X. Sun, A. M. Stavola, D. Cao, A. M. Bruck, Y. Wang, Y. Zhang, P. Luan, J. W. Gallaway, H. Zhu, *Adv. Energy Mater.* **2021**, *11*, 2002861.
[3] Y. Zhu, X. He, Y. Mo, *ACS Appl. Mater. Interfaces* **2015**, *7*, 23685.
[4] D. Cao, Y. Zhao, X. Sun, A. Natan, Y. Wang, P. Xiang, W. Wang, H. Zhu, *ACS Energy Lett.* **2020**, *5*, 3468.
[5] *Mineral Commodity Summaries*, US Geological Survey, Reston, VA, USA **2021**, p. 200.
[6] J. Lu, Z. Chen, F. Pan, Y. Cui, K. Amine, *Electrochem. Energy Rev.* **2018**, *1*, 35.
[7] B. Zhu, X. Wang, P. Yao, J. Li, J. Zhu, *Chem. Sci.* **2019**, *10*, 7132.
[8] X.-B. Cheng, R. Zhang, C.-Z. Zhao, Q. Zhang, *Chem. Rev.* **2017**, *117*, 10403.
[9] a) T. Krauskopf, F. H. Richter, W. G. Zeier, J. Janek, *Chem. Rev.* **2020**, *120*, 7745; b) O. Sheng, J. Zheng, Z. Ju, C. Jin, Y. Wang, M. Chen, J. Nai, T. Liu, W. Zhang, Y. Liu, X. Tao, *Adv. Mater.* **2020**, *32*, 2000223.
[10] D. Cao, X. Sun, Q. Li, A. Natan, P. Xiang, H. Zhu, *Matter* **2020**, *3*, 57.
[11] M. Ashuri, Q. He, L. L. Shaw, *Nanoscale* **2016**, *8*, 74.
[12] X. Su, Q. Wu, J. Li, X. Xiao, A. Lott, W. Lu, B. W. Sheldon, J. Wu, *Adv. Energy Mater.* **2014**, *4*, 1300882.
[13] a) J. Trevey, J. S. Jang, Y. S. Jung, C. R. Stoldt, S.-H. Lee, *Electrochem. Commun.* **2009**, *11*, 1830; b) N. A. Dunlap, S. Kim, J. J. Jeong, K. H. Oh, S.-H. Lee, *Solid State Ionics* **2018**, *324*, 207; c) D. M. Piper, T. A. Yersak, S.-H. Lee, *J. Electrochem. Soc.* **2012**, *160*, A77.
[14] a) R. Miyazaki, N. Ohta, T. Ohnishi, I. Sakaguchi, K. Takada, *J. Power Sources* **2014**, *272*, 541; b) R. B. Cervera, N. Suzuki, T. Ohnishi, M. Osada, K. Mitsuishi, T. Kambara, K. Takada, *Energy Environ. Sci.* **2014**, *7*, 662.
[15] D. H. S. Tan, Y.-T. Chen, H. Yang, W. Bao, B. Sreenarayanan, J.-M. Doux, W. Li, B. Lu, S.-Y. Ham, B. Sayahpour, J. Scharf, E. A. Wu, G. Deysher, H. E. Han, H. J. Hah, H. Jeong, J. B. Lee, Z. Chen, Y. S. Meng, *Science* **2021**, *373*, 1494.

© 2022 Wiley-VCH GmbH

[16] Y. Wang, T. Liu, J. Kumar, *ACS Appl. Mater. Interfaces* **2020**, *12*, 34771.
[17] J.-M. Doux, H. Nguyen, D. H. S. Tan, A. Banerjee, X. Wang, E. A. Wu, C. Jo, H. Yang, Y. S. Meng, *Adv. Energy Mater.* **2020**, *10*, 1903253.
[18] M. A. Hopcroft, W. D. Nix, T. W. Kenny, *J. Microelectromech. Syst.* **2010**, *19*, 229.
[19] M. Yamamoto, Y. Terauchi, A. Sakuda, M. Takahashi, *J. Power Sources* **2018**, *402*, 506.
[20] a) W. Wang, P. N. Kumta, *ACS Nano* **2010**, *4*, 2233; b) C. K. Chan, H. Peng, G. Liu, K. McIlwrath, X. F. Zhang, R. A. Huggins, Y. Cui, *Nat. Nanotechnol.* **2008**, *3*, 31.
[21] M. K. Datta, P. N. Kumta, *J. Power Sources* **2009**, *194*, 1043.
[22] F. Sun, K. Dong, M. Osenberg, A. Hilger, S. Risse, Y. Lu, P. H. Kamm, M. Klaus, H. Markötter, F. García-Moreno, T. Arlt, I. Manke, *J. Mater. Chem. A* **2018**, *6*, 22489.
[23] W. Zhang, D. A. Weber, H. Weigand, T. Arlt, I. Manke, D. Schröder, R. Koerver, T. Leichtweiss, P. Hartmann, W. G. Zeier, J. Janek, *ACS Appl. Mater. Interfaces* **2017**, *9*, 17835.
[24] a) Y. Liu, Y. Wu, J. Zheng, Y. Wang, Z. Ju, G. Lu, O. Sheng, J. Nai, T. Liu, W. Zhang, X. Tao, *Nano Energy* **2021**, *82*, 105723; b) Z. Ju, C. Jin, H. Yuan, T. Yang, O. Sheng, T. Liu, Y. Liu, Y. Wang, F. Ma, W. Zhang, J. Nai, X. Tao, *Chem. Eng. J.* **2021**, *408*, 128016.
[25] Y. Zhang, X. Sun, D. Cao, G. Gao, Z. Yang, H. Zhu, Y. Wang, *Energy Storage Mater.* **2021**, *41*, 505.
[26] C. Wang, J. Liang, Y. Zhao, M. Zheng, X. Li, X. Sun, *Energy Environ. Sci.* **2021**, *14*, 2577.
[27] a) D. Cao, Y. Zhang, A. M. Nolan, X. Sun, C. Liu, J. Sheng, Y. Mo, Y. Wang, H. Zhu, *Nano Lett.* **2020**, *20*, 1483; b) J. Janek, W. G. Zeier, *Nat. Energy* **2016**, *1*, 16141; c) S. P. Culver, R. Koerver, W. G. Zeier, J. Janek, *Adv. Energy Mater.* **2019**, *9*, 1900626.
[28] S. Schweidler, L. de Biasi, G. Garcia, A. Mazilkin, P. Hartmann, T. Brezesinski, J. Janek, *ACS Appl. Energy Mater.* **2019**, *2*, 7375.
[29] H.-H. Ryu, K.-J. Park, C. S. Yoon, Y.-K. Sun, *Chem. Mater.* **2018**, *30*, 1155.
[30] R. Ruess, S. Schweidler, H. Hemmelmann, G. Conforto, A. Bielefeld, D. A. Weber, J. Sann, M. T. Elm, J. Janek, *J. Electrochem. Soc.* **2020**, *167*, 100532.
[31] A. Sakuda, A. Hayashi, M. Tatsumisago, *Chem. Mater.* **2010**, *22*, 949.
[32] a) X. Liu, B. Zheng, J. Zhao, W. Zhao, Z. Liang, Y. Su, C. Xie, K. Zhou, Y. Xiang, J. Zhu, H. Wang, G. Zhong, Z. Gong, J. Huang, Y. Yang, *Adv. Energy Mater.* **2021**, *11*, 2003583; b) C. Wang, R. Yu, S. Hwang, J. Liang, X. Li, C. Zhao, Y. Sun, J. Wang, N. Holmes, R. Li, H. Huang, S. Zhao, L. Zhang, S. Lu, D. Su, X. Sun, *Energy Storage Mater.* **2020**, *30*, 98.
[33] C. Doerrer, I. Capone, S. Narayanan, J. Liu, C. R. M. Grovenor, M. Pasta, P. S. Grant, *ACS Appl. Mater. Interfaces* **2021**, *13*, 37809.
[34] X. Dong, J. Yao, W. Zhu, X. Huang, X. Kuai, J. Tang, X. Li, S. Dai, L. Shen, R. Yang, L. Gao, J. Zhao, *J. Mater. Chem. A* **2019**, *7*, 20262.
[35] D. Cao, Q. Li, X. Sun, Y. Wang, X. Zhao, E. Cakmak, W. Liang, A. Anderson, S. Ozcan, H. Zhu, *Adv. Mater* **2021**, *33*, 2105505.
[36] Z. Zeng, N. Liu, Q. Zeng, S. W. Lee, W. L. Mao, Y. Cui, *Nano Energy* **2016**, *22*, 105.
[37] A. Gupta, S. Hartner, H. Wiggers, in *2010 3rd Int. Nanoelectronics Conf. (INEC)*, IEEE, Piscataway, NJ, USA **2010**, pp. 616–617.
[38] L. Han, T. Liu, O. Sheng, Y. Liu, Y. Wang, J. Nai, L. Zhang, X. Tao, *ACS Appl. Mater. Interfaces* **2021**, *13*, 45139.
[39] F. Hippauf, B. Schumm, S. Doerfler, H. Althues, S. Fujiki, T. Shiratsuchi, T. Tsujimura, Y. Aihara, S. Kaskel, *Energy Storage Mater.* **2019**, *21*, 390.

© 2022 Wiley-VCH GmbH